QR/1997/2

AIAA 97-0722

The Differentially Heated, Rotating Cylindrical Annulus: A Numerical Simulation

D. Baeza and S. Ahmed
Parks College of Saint Louis University
Cahokia, Illinois

B. G. Sherlock
University of Bath
Bath, U.K.

Q. G. Rayer
Nuclear Electric Plc., Berkeley Technology Center
Gloucestershire, U.K.

35th Aerospace Sciences Meeting & Exhibit
January 6-10, 1997 / Reno, NV

AIAA-97-0722-

THE DIFFERENTIALLY HEATED, ROTATING CYLINDRICAL ANNULUS: A NUMERICAL SIMULATION

D. Baeza and S. Ahmed
Parks College of St. Louis University, Cahokia Il 62206

B. G. Sherlock
University of Bath, BA2 7AY, UK

Q. G. Rayer
Nuclear Elec. Plc, Berkeley Technology Centre, GL13 9PB, UK

Abstract

Rotating, differentially heated cylindrical annulus systems present a simple way of modeling the basic qualitative phenomena in atmospheric and oceanic flows. Non-rotating systems are useful in studying nuclear fuel cooling containers, thermal storage devices and inert gas cooled cables. Recently, detailed experimental measurements were obtained by Q. G. Rayer[1] for a rotating cylindrical annulus with walls maintained at different temperatures and blocked by an adiabatic radial barrier. Rayer's experimental data is compared with the numerical simulation, which uses a control volume formulation of the Navier Stokes equations and assumes a Boussinesq fluid. The discretized equations are solved using a SIMPLE-like algorithm. Results for low rotation rates show a vertical flow cell with fluid rising along the hotter outer wall, traveling radially inward at the top and sinking at the cooler inner wall. An azimuthal cell is also present, which circulates in the same sense as the rotation rate near the bottom and transitions to the inverse sense near the top. Increasing the rotation rate causes the flow to become unstable and large eddies to appear. Results for the pressure field are provided, verifying earlier hypotheses of radial and azimuthal geostrophic flow. Predicted heat transfer rates agree well with experimental results.

Nomenclature

A, B, C, D, E, F: Nondimensional parameters.
a: Radius of inner annulus wall.
b: Radius of outer annulus wall.
C_p: Specific heat capacity of fluid.
g: Gravitational acceleration vector, $\mathbf{g} = -g\hat{k}$
k: Thermal conductivity of fluid.
K: Constant to adjust reference velocity,
L: Height of annulus.
$\hat{e}_r, \hat{e}_\theta, \hat{k}$: Radial, azimuthal and vertical unit vectors of cylindrical coordinate system,
Nu: Nusselt number.
p: Pressure field.
Pr: Prandtl number.
Q: Heat transfer through boundaries.
Ra: Rayleigh number.
(r,θ,z): Cylindrical coordinates.
T: Temperature field.
T_{wh}: Highest of T_a and T_b.
$\mathbf{V}$: Fluid velocity, with components (u,v,w).
α: Thermal expansion coefficienty.
β: Thermometric conductivity.
μ: Absolute viscosity of fluid.
ν: Kinematic viscosity of fluid.
ρ: Density of fluid.
τ: Taylor number.
ΔP_b: Pressure jump across radial barrier.
ΔT: Temperature difference between walls.
ΔT_b: Temperature jump across radial barrier.
Θ: Rossby number.
Ω: Angular velocity of system, $\Omega = \omega\hat{k}$.
$()_a$, $()_b$: Denote properties at inner and outer walls.
$()_0$: Denotes reference values.
$()^*$: Denotes non-dimensional variable.

Introduction

Considerable attention has been given in the past to differentially heated, rotating and non-rotating cylindrical annulus systems. Applications of non-rotating systems include nuclear reactor cooling, nuclear fuel cooling containers, thermal storage systems, solar collectors and inert-gas insulated electrical cables[2]. Rotating cylindrical annulus systems reproduce many of the global qualitative aspects of natural convection systems encountered in stellar and planetary cores, ocean currents and atmospheres. In these cases, the rotation around the system's longitudinal axis mimics the effects of planetary

rotation by introducing Coriolis and centrifugal forces. Although by no means a model of the atmosphere, the cylindrical annulus system is simple enough to be modeled, while still being an elementary analogue to the essential dynamic processes existing in the atmosphere. Some of the processes that may be simulated are geostrophic flow, thermal winds, baroclinic and barotropic instabilities, Hadley cells, Rossby waves, etc.[3]

The basic phenomena observed in the unblocked, rotating annulus are the three distinct flow regimes determined by ω and ΔT. For a typical $\Delta T \approx 10K$ there is axisymmetric flow at low rotation rates ($\omega \approx 0.4 rad/s$), regular waves at moderate rotation rates ($1 < \omega < 3.5$ *rad/s* approx.) and irregular, aperiodic flow for higher values of ω. Also, another axisymmetric regime occurs at all values of ω if ΔT is sufficiently small. The reader is referred to Read,[2] Fowlis and Hide,[4] Williams,[5] and Busse[6]. For blocked annulus flow, the regimes are different: regular waves are not observed and instead, large eddies and irregularities start to appear in the flow above certain values of ω and ΔT. To include the effects of different fluid properties and geometries, the flow regimes are better classified according to two parameters, the thermal Rossby number and the Taylor number, $\Theta = \alpha g L \Delta T / [\omega^2 (b-a)^2]$ and $\tau = 4\omega^2 (b-a)^5 / (\nu^2 L)$ respectively, which were first suggested by Robinson[7] and Fowlis and Hide. Flow regime diagrams for annular systems as a function of Θ and τ are common in the literature.

In the regimes described above the main driving force is the buoyancy due to gravity, acting parallel to the axis of rotation. The resulting flow is geostrophic in nature and takes the form of a meridional or Hadley cell, with fluid rising at the hot outer wall and sinking at the cooler inner wall. This flow regime is applicable to the study of atmospheric phenomena such as trade winds, thermal cyclones or meridional circulation, which is the main form of heat transport in equatorial regions.

Regarding heat transfer rates, it has been shown experimentally that for an unblocked annulus, increasing the rotation rate markedly decreases heat advection, the net heat transfer through the annulus and *Nu*, see for example Bowden and Eden [8]. It was then hypothesized that blocking the fluid annulus with a thin radial barrier would enable an azimuthal temperature and pressure gradient to form, resulting in radial geostrophic flow and making the heat advection independent of ω. Experimental heat transfer results obtained by Bowden and Eden[9] and Rayer[1] have confirmed this fact. Radial barriers that do not extend the full height of the cylinder are useful in understanding topographical obstructions to atmospheric flow, such as the Antarctic Circumpolar Current, as suggested by Fultz[10] and Rayer.[1]

Description Of Cylindrical Annulus System Used In This Study

Since one of the objectives is to validate the numerical model by comparison to experimental data, the system modeled is exactly that employed by Rayer and is shown in Fig. 1. The fluid-filled annulus (a = 2.5 *cm*, b = 8 *cm*, L = 14 *cm*) is able to rotate about its longitudinal axis with a constant angular velocity Ω. The inner and outer heat conducting boundaries are kept at temperatures T_a and T_b respectively (with $T_a < T_b$), and such that the mean of the two temperatures remains fixed at 293.15 K for all cases. The upper and lower boundaries are adiabatic. The annulus is blocked by a radial adiabatic barrier at $\theta = 0$. The fluid properties are shown in Table 1 and correspond to a water-glycerol solution, as used by Rayer.[1]

ρ	$1045\ Kg \cdot m^{-3}$
μ	$1.81\times10^{-3}\ Kg \cdot s^{-1} \cdot m^{-1}$
C_p	$3.84\times10^{+3}\ J \cdot Kg^{-1} \cdot K^{-1}$
α	$3.03\times10^{-4}\ K^{-1}$
k	$0.518\ W \cdot m^{-1} K^{-1}$

Table 1: Fluid properties (water-glycerol mixture).

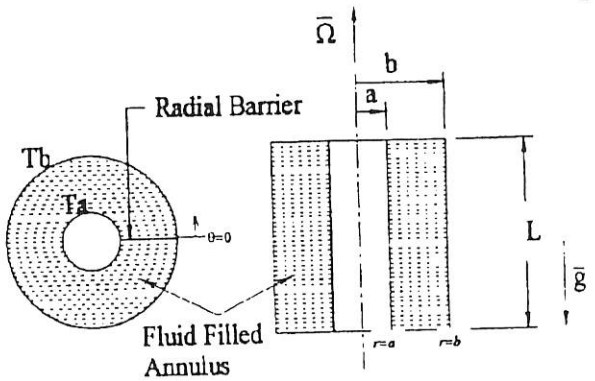

Figure 1: Schematic of the cylindrical annulus convection chamber. The top and bottom walls as well as the radial barrier are adiabatic and Ta < Tb.

Governing Equations

The following assumptions have been made in deriving the conservation equations that describe the system of interest:[11]

1. Constant viscosity ν, thermal conductivity α and coefficient of thermal expansion β.
2. Incompressible flow ($\nabla \cdot \mathbf{V} \approx 0$).
3. Newtonian fluid obeying Fourier's heat transfer law.
4. Rotating (non-inertial) reference frame with angular velocity $\Omega = \omega \hat{k}$ and gravity the only body force, given as $\mathbf{g} = -g\hat{k}$.

The conservation equations as adapted to this particular problem then become:

Conservation of Mass

$$\nabla \cdot \mathbf{V} \approx 0 \tag{1}$$

Conservation of Linear Momentum

$$\frac{\partial}{\partial t}(\rho \mathbf{V}) + \nabla \cdot (\rho \mathbf{V}\mathbf{V}) = -\nabla p - \rho g \hat{k} + \mu \nabla^2 \mathbf{V} - \rho\left[\Omega \times (\Omega \times \mathbf{r}) + 2\Omega \times \mathbf{V}\right] \tag{2}$$

Conservation of Energy

$$\rho c_p \frac{DT}{Dt} = \beta T \frac{Dp}{Dt} + k\nabla^2 T + \Phi \tag{3}$$

For low speed flows where heat transfer is the predominant phenomena, the dissipation Φ and the pressure contribution Dp/Dt may be assumed very small compared to the rest of the terms of Eq. 3 and therefore both terms will be neglected in the analysis. Neglecting these terms has been the usual practice in past studies of similar systems, see for example White,[12] Fultz,[13] Robinson[14] and Randiamampianina.[15] Conceptually though, these two terms are important because they represent the two transfer terms by means of which the system works as a thermodynamic engine. In the numerical experiments performed herein, the contribution of the dissipation term was verified to be negligible.

A linear dependence of density on temperature is assumed, providing the equation of state

$$\rho = \rho_0[1 - \alpha(T - T_0)] \tag{4}$$

where ρ_0 is a reference value for density. In the derivation of the non-dimensionalized equations, it is assumed that the coefficient of thermal expansion in Eq. (4) is zero (that is, $\rho^* = 1$) except when coupled with the gravitational, centrifugal or Coriolis terms. These two last assumptions, along with incompressibility comprise the Boussinesq approximation, which is generally assumed valid for maximum temperature variations of 10 K within the fluid.[5] Eqs. (1) through (4) form a system of six equations with six unknowns: $\mathbf{V}$, p, T, and ρ.

If a set of non-dimensional variables valid for the special cases $\omega = 0$ and $T_a^* = T_o$ is desired, the reference values used in the non-dimensionalization must be independent of ω and $(T_a - T_b)$ to avoid singularities. This represents an improvement over the previous models of Mukira[2] and Ahmed.[16] Thus, the reference time and velocity were chosen as $V_0 = K(\alpha g T_{wh} L)^{1/2}$ and $t_0 = L/V_0$, where K is a constant to adjust the velocity and time scales for different fluid properties, wall temperatures, geometry and equilibrium times. By incorporating T and α, this new choice of reference variables is coherent with the fact that this is mainly temperature-driven flow. For the present model, setting K = 1/100 yielded a reference velocity $V_0 = 2.1$ *mm/s* and a reference time of $t_0 = 24$ *s*, comparable in magnitude to the observed maximum velocities and equilibrium time, about 10 *mm/s* and 850 *s* respectively.

With V_0, t_0, ρ_0 and μ_0 as the reference values, the non-dimensional variables are

$$\mathbf{V}^* = \frac{\mathbf{V}}{V_0},\ x_i^* = \frac{x_i}{L},\quad t^* = \frac{t}{t_0},\quad \alpha^* = \alpha T_{wh},$$

$$\mu^* = \frac{\mu}{\mu_0},\quad \rho^* = \frac{\rho}{\rho_0},\quad T^* = \frac{T - T_0}{T_{wh}} \text{ and}$$

$$p^* = \frac{p - \rho_0 g(L - z) - \frac{1}{2}\rho_0 \omega^2 r^2}{\rho_0 V_0^2}.$$

Equations (5) through (7) are the nondimensionalized conservation laws.

Conservation of Mass

$$\nabla^* \cdot \mathbf{V}^* \approx 0 \tag{5}$$

Conservation of Linear Momentum

$$\frac{\partial}{\partial t^*}\mathbf{V}^* + \nabla^*(\mathbf{V}^*\mathbf{V}^*) = -\nabla^* p^* + \underbrace{\frac{1}{K^2}}_{A} T^* \hat{k}$$

$$-\underbrace{\left(\frac{\omega L^2}{K\sqrt{\alpha g T_{wh} L}}\right)^2}_{B^2} \alpha^* r^* T^* \hat{e}_r - 2\underbrace{\left(\frac{\omega L^2}{K\sqrt{\alpha g T_{w,h} L}}\right)}_{B}(1-\alpha^* T^*) \times$$

$$(u^* \hat{e}_\theta - v^* \hat{e}_r) + \underbrace{\frac{\mu_0}{KL\rho_0\sqrt{\alpha g T_{w,h} L}}}_{C} \nabla^{*2}\mathbf{V} \qquad (6)$$

Conservation of Energy

$$\rho^* c_p^* \left[\frac{\partial T^*}{\partial t^*} + (\mathbf{V}^* \cdot \nabla^*) T^*\right] = \underbrace{\frac{k_0}{c_{p0}\rho_0 KL\sqrt{\alpha g T_{wh} L}}}_{D} k^* \nabla^{*2} T^*$$

$$+ \underbrace{\frac{\mu_0}{\rho_0 c_{p0} T_{wh}}}_{E} \mu^* \Phi^* - \underbrace{\frac{\omega^2 L^2}{C_{p0} T_{wh}}}_{F} \rho^* u^* r^* \qquad (7)$$

The equation of state takes the non-dimensional form

$$\rho^* = 1 - \alpha^* T^* \qquad (8)$$

The non-dimensional numbers appearing in these equations will be referred to as A, B, C and D, E and F.

Discretization Of Conservation Equations

A control volume formulation and a staggered grid was used for the discretization of the momentum equation (Eq. 6) which ensures that momentum is exactly conserved over the computational domain.[17] The momentum fluxes at the cell faces were specified by using first order upwinding. A central difference representation for velocity gradients at the cell faces was employed when the viscous terms in the momentum equation were discretized.

The generic volume element used to discretize the r-momentum equation centered on the grid location $(i+½,j,k)$ is shown in Fig. 2. In the staggered grid arrangement, the pressure and temperature are specified at locations (i,j,k), while the u, v and w components of velocity are specified at the locations $(i+½,j,k)$, $(i,j+½,k)$ and $(i,j,k+½)$ respectively. The control volumes used to discretize the θ-momentum and the z-momentum equations are centered on $(i,j+½,k)$ and $(i,j,k+½)$ respectively. Thus when using a staggered grid, the velocity at a point (i,j,k) depends on the surrounding pressures one-half a cell width away, which is a good analogue to reality. The resulting numerical scheme is explicit and formally first order accurate.

The governing equations, which are a mixed set of parabolic and elliptical equations were solved explicitly using a time marching technique. The solution algorithm used is the SIMPLE procedure (Semi-Implicit Method for Pressure Linked Equations) introduced by Patankar and Spalding[17].

The computational grid is shown in Fig. 3. The number of cells used were 15 in the radial direction, 31 in the azimuthal and 15 in the axial direction. However this is reduced to 13, 39 and 13 respectively since the outermost cell in each direction was not part of the physical domain, but was needed to implement the boundary conditions. A logarithmic

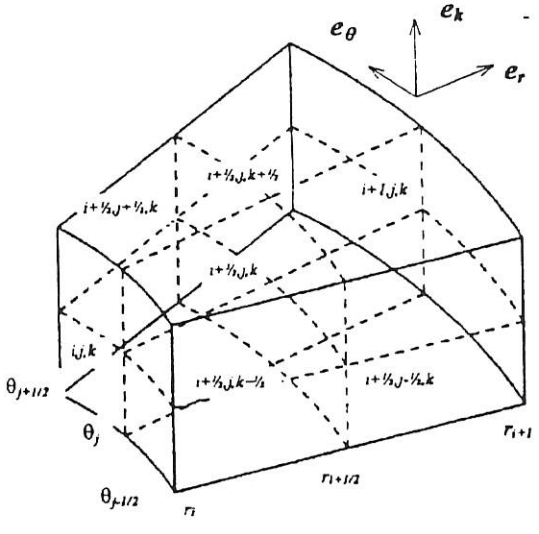

Figure 2: Control volume used to discretize the r-momentum equation.

Roberts transformation[17] was used to refine the grid in the proximity of the boundaries. Factors determining the grid size were the available computing power and the fact that 10 different cases were to be analyzed. Upon comparison of the present results with previous work using a grid with roughly double the number of gridpoints in each direction (Ahmed[16]), it was concluded that the solutions obtained were grid independent for this resolution range.

Initial pressure distribution is obtained by solving the Poisson equation for pressure. The no-slip boundary condition is applied to all solid surfaces of

the enclosure. The boundary conditions for pressure are obtained by evaluating the appropriate component of the conservation of momentum equation for each boundary. Marching in time continues until the changes in flow variables are sufficiently small to ensure that a steady state has been reached. Typically, this occurred after 850 seconds.

Results And Comparison With Experimental Data

For a radially blocked annulus, a stable regime is found for low rotation rates while an unstable flow regime, characterized by eddies, is found at the higher values of ω and ΔT. Table 2 below summarizes the different cases that were modeled in this study, indicating the flow

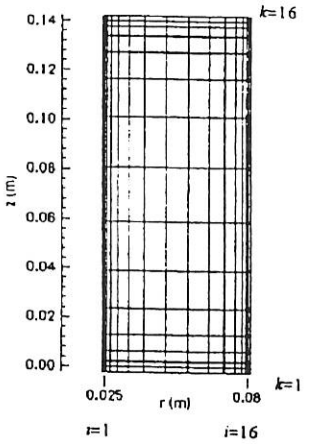

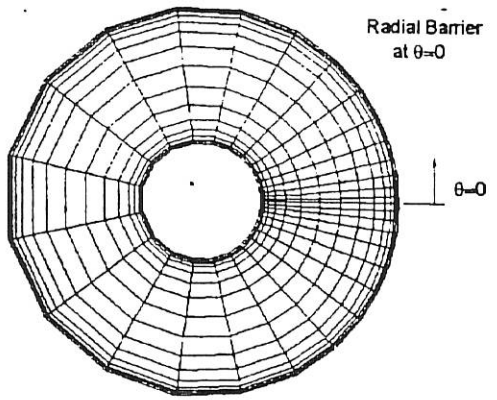

Figure 3: Computational grid in the (r, z) and (r, θ) planes.

regime observed (eddies/no eddies). For conciseness, detailed results are only included for cases 6, 7 and 10, corresponding to $\Delta T = 10\ K$.

Case No.	ω rad/s	ΔT °C	τ	Θ	Flow Type
1	0	4	0	∞	No eddies
2	0.2	4	1.92×10^{5}	13.75	No eddies
3	0.5	4	1.20×10^{6}	2.201	No eddies
4	1.7	4	9.39×10^{6}	0.281	No eddies
5	4	4	7.67×10^{7}	0.034	No eddies
6	0	10	0	∞	No eddies
7	0.4	10	7.67×10^{5}	8.598	No eddies
8	1.2	10	6.90×10^{6}	0.955	No eddies
9	1.7	10	1.39×10^{7}	0.476	No eddies
10	4	10	7.67×10^{7}	0.086	Eddies

Table 2: Summary of cases studied. ($Pr = 14$)

A simplified, qualitative picture of a typical flow pattern for low rotation rates and low ΔT is shown in Figure 4. In this simplified picture, two circulation cells may be distinguished: a radial, Hadley-type cell and an azimuthal cell. The basic radial cell is confined to the vicinity of the walls. Buoyancy causes the fluid to ascend by the hot outer wall, at the top of the chamber the fluid travels radially inwards before descending by the cool inner wall at a slightly increased velocity.

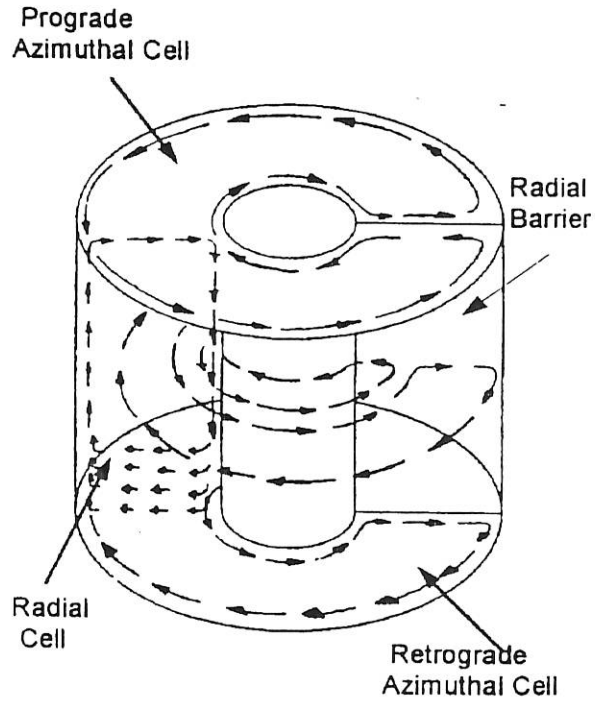

Figure 4: Simplified diagram of computed flow for low ω and ΔT, showing the radial cell and the azimuthal cell.

In the model, the azimuthal cell depends on z, contrary to the experimental results of Rayer.[1] From the lower boundary to about $^2/_3L$ the flow in the azimuthal cell has the opposite sense as the rotation Ω, which will be referred to as retrograde flow. At around $^2/_3L$ the prograde flow along the inner boundary, starts to become important and will predominate in the upper third of the annulus. Momentum balance dictates that the retrograde velocities in the bottom 2/3 of the chamber must be lower than the prograde velocities in the upper third of the annulus. The basic flow just described shows important variations depending on the values of ω which are described in subsequent sections.

Velocity Vector Diagram

For $\omega = 0$, inspection of Fig. A.1 in the Appendix reveals practically zero azimuthal velocity except near the radial barrier, where the associated boundary layer causes the flow to deviate slightly from being fully axisymmetric. There is a strong radial inward flow at the top of the cylinder, from the cool wall to the hot inner wall. The outward radial flow at the bottom of the cylinder is not as strong and takes place in the region $2\ cm < z < 6\ cm$. The velocity profiles in the (r, z) plane of Figure A.2 show the radial cell clearly. As expected, this special case with no rotation shows practically zero azimuthal velocities.

When rotation is introduced, the Coriolis acceleration that acts on the fluid particles with non-zero radial velocity imposes an azimuthal velocity to the flow, and the system behaves as shown previously in Fig. 4. For $\omega = 0.4\ rad/s$ (Fig. A.3) large eddy formations are observed near the radial boundary at $\theta \approx 330°$. However, away from influence of the radial barrier (Fig. A.4, at $\theta = 180°$) nearly zero vertical velocities are found, satisfying the Taylor-Proudman theorem. Upon increasing the rotation rate to $\omega = 4\ rad/s$ the flow becomes unstable and eddies start appearing in regions far away from the radial barrier. At this high rotation rate, the Hadley cell appears severely modified, with large eddies occurring in its inner domain (Fig. A.5). To further illustrate the flow, Fig. A.6 was constructed by overlaying azimuthal velocity contours on the velocity vector plot for $\theta = 180°$, opposite the radial barrier.

Experimental results obtained by Rayer for ω=0.4 *rad/s* and ΔT=10 K are shown in Fig. A.7. Note that the azimuthal cell has a prograde sense of rotation throughout the annulus and becomes very weak near the top, where the flow proceeds radially inward [Fig. A.7]. The predicted velocities in the inner domain of the annulus are sometimes 2 to 3 times larger than measured velocities. The model also predicts a strong prograde flow near the inner cylinder and near the wall at $\theta = 2\pi$, for which there is no experimental evidence. It could be argued that measurements were not taken in the immediate vicinity of the inner cylinder, but still there is no hint of this prograde flow in the adjacent flow layers. Thus it seems that the overall prediction of the flow, although logical in nature, does not match experimental results fully.

Transition to Eddy Flow

It was previously mentioned that eddies start appearing in blocked annulus flows at the higher values of ω and ΔT. Experimental results by Rayer [1] conclude that the transition to this unstable eddy regime for this particular system occurs in the interval $1.176 < \omega < 1.372\ rad/s$ for $\Delta T = 4K$ and in the interval $1.196 < \omega < 1.697\ rad/s$ for $\Delta T = 10K$. The computer model was tested up to $\omega = 4 rad/s$ for $\Delta T = 4K$ but no eddies other than those near the radial barrier were found. For $\Delta T = 10K$, eddies first occurred somewhere in the interval at $2 < \omega < 4\ rad/s$. It is anticipated that using a finer grid may provide a better correlation with experimental results in predicting the transition to the eddy regime.

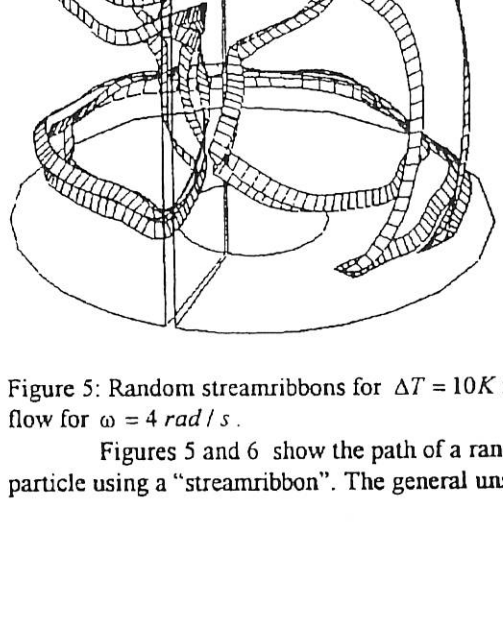

Figure 5: Random streamribbons for $\Delta T = 10K$; unstable flow for $\omega = 4\ rad/s$.

Figures 5 and 6 show the path of a random fluid particle using a "streamribbon". The general unstable

nature of the flow for $\omega = 4\ rad/s$ may be observed in Fig. 5 which also shows a large eddy away from the radial barrier, at $\theta \approx 200\ deg$. Figure 6 depicts a random streamribbon for $\omega = 0.4\ rad/s$; the flow is stable and no eddies are present except near the radial barrier.

Temperature Distribution Results

Results are provided in Fig. A.8 for the isotherms at $\theta = 180°$ and $\theta = 358°$ obtained from the energy equation. Isotherms are approximately horizontal in the lower third of the annulus. Near the top, the highly sloped isotherms reflect the hotter and faster moving fluid sinking and cooling. Moderate rotation seems to lessen this effect and the isotherms appear closer to horizontal with $\partial T/\partial z$

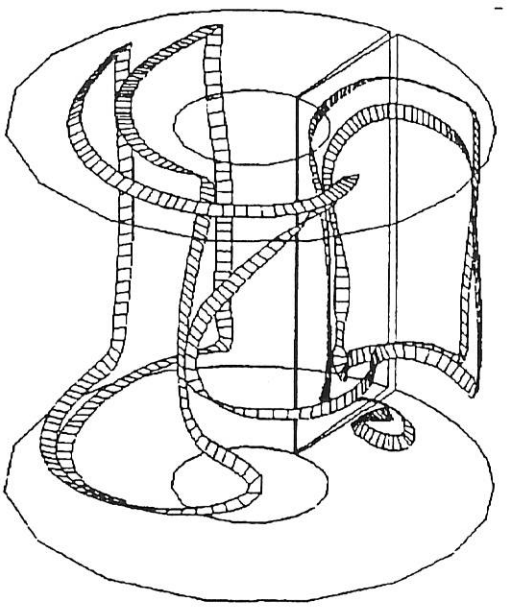

Figure 6: Random streamribbons for $\Delta T = 10K$; stable flow for $\omega = 0.4\ rad/s$.

approximately constant at mid-radius and $\theta = 180°$. At higher rotation rate the irregular sawtooth temperature contours corresponding to the eddy forms. These irregular contours are not only present in the outer boundaries, but throughout the inner domain of the fluid as well.

No detailed experimental temperature profiles have been found to contrast with computed data, however Rayer[1] and Bowden and Eden[9] did conduct temperature measurements at mid-radius and mid-depth for $0 < \theta < 2\pi$ using a circular ring of thermocouples. The equivalent computed results are shown in Fig. A.9. For zero rotation rate this profile is symmetrical with respect to θ=180°, as expected, and thus the temperature is equal on both sides of the radial barrier. As the rotation rate is increased, computed results show an azimuthal temperature gradient developing. Hotter fluid concentrates near the radial barrier at $\theta = 2\pi$, and cooler fluid on the opposite side ($\theta = 0$). A temperature jump denoted by ΔT_b is established between both sides of the thermally insulated radial wall with values given in Table 3. It is seen that ΔT_b increases with the rotation rate, but the results obtained by Rayer indicate a ΔT_b of lower magnitude. Bowden and Eden reported for a similar system a temperature jump of $\Delta T_b = 1.1\ K$, which is somewhat closer to the results presented here. Rayer observed that in his experiment the spacing of the thermocouples was not fine enough to give good resolution within the thermal boundary layer of the radial barrier. Thus, computed results correspond to locations closer to the barrier than experimental results and a direct comparison is not possible. Rayer estimated that truncating computational results to match the thermocouple locations would give $\Delta T_b = 0.44\ K$ for $\omega = 0.4\ rad/s$ and $\Delta T = 10\ K$, but still computed results for ΔT_b would roughly double the experimental temperature jumps.

Case	ω (rad/s)	ΔT (°C)	$\Delta T_b(K)$ Computed	$\Delta T_b(K)$ Experimental (±0.014)
1	0	4	≈ 0	0.03
3	0.5	4	0.98	0.16(*)
4	1.7	4	2.95	0.60
7	0.4	10	0.96	0.15
10	4	10	4.51	1.97

Table 3: Temperature drop across the thermally insulated radial barrier. Experimental results are from Rayer[1] with an asterisk indicating extrapolated values.

Balance of Terms in the Momentum Equation:

A deeper understanding of the flow may be gained by plotting the relative size of each term in the non-dimensionalized momentum equation (Eq. 6) versus r, θ and z.

For zero angular velocity, the radial and azimuthal equations present a balance between the combined pressure and viscous forces and the advection forces. The viscous term is significant in the interior of the fluid in this flow regime. The advection term is also considerable in all three components of the momentum equation. Thus, models

of the non-rotating annulus system that do not include viscous effects are not expected to be accurate. The vertical equation of motion (Fig. A.11) shows hydrostatic balance, with advection terms being of secondary importance. In the rotating system with $\omega = 0.4\ rad/s$, both the radial and azimuthal momentum equations (Fig. A.12) show approximate geostrophic balance throughout the interior of the fluid, outside of the boundary layers. A geostrophic balance implies equilibrium between the Coriolis and the pressure gradient forces, the resulting steady flow being parallel to the isobars. Figures A.13 and A.14 show an Ekman boundary layer at the top, bottom and cylindrical boundaries of the annulus, which involves equilibrium between the Coriolis, pressure gradient and viscous forces.

The vertical velocity equation (Fig. A.14) presents hydrostatic balance between the pressure and buoyancy forces, except in the boundary layer near the inner cylinder, where the viscous terms is significant. Thus, the vertical motions in the fluid are almost exclusively buoyancy driven. For $\omega = 4\ rad/s$, the geostrophic balance is broken by the increased magnitude of the centrifugal forces in the outer third of the annulus. At this high rotation rate, the instabilities present in the flow are reflected in the oscillations that occur in the vertical and azimuthal components of the momentum equation, Fig. A.15.

Balance of Terms in the Energy Equation

In order to determine the relative importance of the viscous dissipation and centrifugal terms of the energy equation, the magnitude of the different terms were compared. This values are plotted for mid-radius, mid-depth and $\theta = \pi$ in Fig. 7. Analysis of this figure reveals that the main contributions to the energy equation come from the advection and the dT/dt terms. Neither the dissipation term nor the centrifugal term are of importance, being of the order of 10^{-8} and 10^{-4} respectively for ω=0.4 *rad/s* and ΔT=10 *K*. However, the magnitude of these terms needs to be investigated for higher rotation rates, as it is possible that they may no longer be negligible.

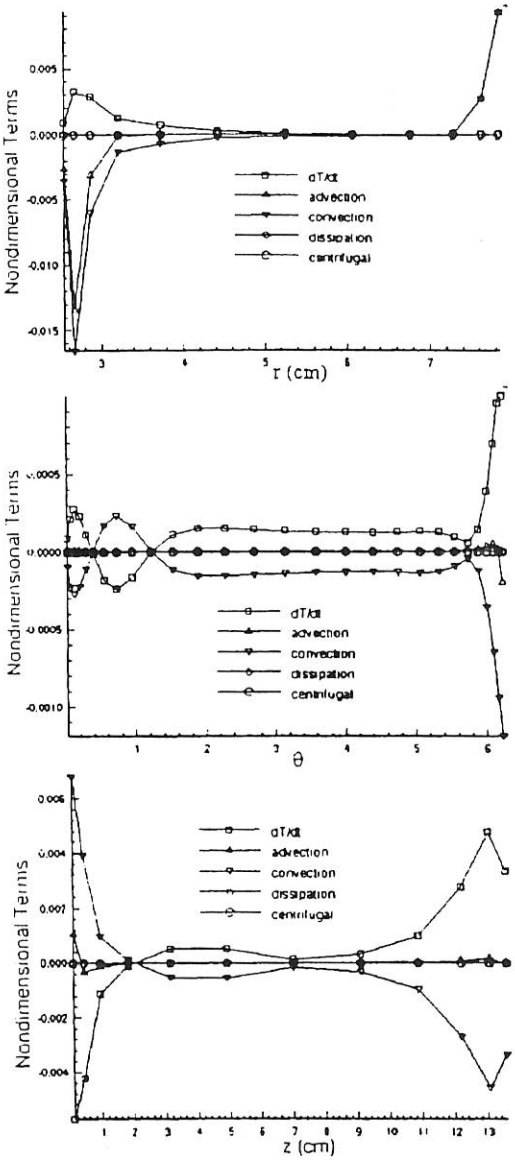

Figure 7: Balance of terms in the non-dimensionalized energy equation for mid-radius, mid-height and $\theta = 180°$ as a function of r, θ and z. (ω=0.4 *rad/s*, ΔT=10 *K*).

Pressure Field Results

The azimuthal pressure gradient shown in figiure A10, is most noticeable near the top of the cylinder but even there is quite weak ($\Delta P_b = 0.23\ Pa$) thus the resulting radial geostrophic flow is also weak. Although not shown, a considerable vertical pressure gradient due to gravity of 1851 *Pa* is also observed.

Heat Transfer Results

Heat transfer rates for the inner and outer cylindrical walls were obtained from the summation of $Q = -dk\,(\partial T/\partial r)_{wall}\,dA$ over the corresponding boundary. A parameter used in comparing heat transfer rates results is the Nusselt number, defined as the ratio of the total heat transfer to the conductive heat transfer, that is,

$Nu = (Q_{adv} + Q_{cond})/Q_{cond} = Q_a/Q_{cond}$, where $Q_{cond} = (2\pi k \Delta T L)/[\ln(b/a)]$ is easily derived assuming a solid annulus with same thermal conductivity as the fluid.

Introducing a fully blocking radial barrier makes the heat transfer rate through the inner cylinder (and thus the Nusselt number) largely independent of ω. Figure 8 shows experimental and computed Nusselt numbers for $\Delta T = 4K$ over a range of rotation rates. Computed results indicate that Nu remains approximately constant for $0 \le \omega \le 0.5$ *rad/s*, then drops about 20% at around $\omega = 1$ *rad/s*, to level off again for $\omega > 1.5$ *rad/s*. According to Rayer however, the Nusselt Number remains constant for $0 < \omega < 4$ *rad/s* and $\Delta T = 4$ *K*, while for ΔT=10 *K* it increases slightly, about 7% from its initial value, by the time 4 *rad/s* is reached.

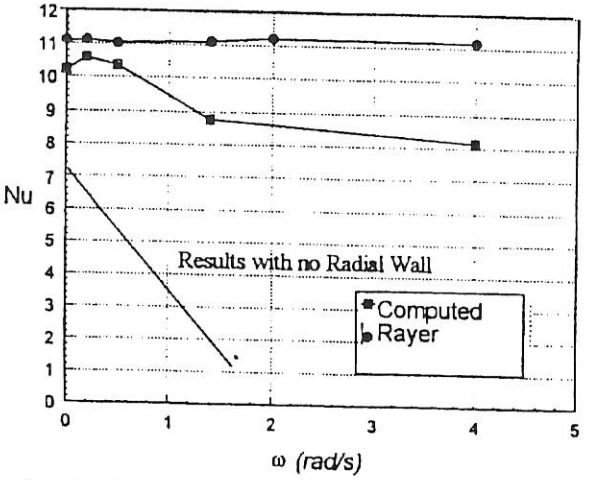

Fig. 8: Experimental and computed Nusselt numbers for $\Delta T = 4K$. Data from Rayer has an error margin of 0.7%.

It is observed that, as the rotation rate increases the advective heat transfer decreases (Table 4). This is so because the conductive heat transfer Q_{cond} is independent of ω and the Nusselt number was found to decrease with increasing rotation rates. Thus increasing ω increases the fraction of heat transfer carried by conduction and decreases advective heat transfer, in agreement with Bowden and Eden.[9]

An interesting check on the accuracy of the heat transfer results is based on the empirical relationship proposed by Bowden (see Rayer[1]), valid for an unblocked annulus. This equation may be applied to the blocked annulus for $\omega = 0$, since the effect of the radial barrier on the flow is minimal in this case. The good agreement between these two results is shown in Table 5.

	ω (*rad/s*)	Nu	Q_{cond} (*W*)	Q_{adv} (*W*)
ΔT=4*K*	0	10.21	1.57	14.43
	0.2	10.60	1.57	15.04
	0.5	10.36	1.57	14.67
	1.4	8.76	1.57	12.16
	4.0	8.12	1.57	10.99
ΔT=10*K*	0	14.18	3.91	51.67
	0.4	13.44	3.91	48.76
	1.2	12.47	3.91	44.97
	1.7	12.06	3.91	43.37
	4.0	10.99	3.91	39.14

Table 4: Computed values of Nusselt number and heat transfer through inner and outer walls.

Case	*Computed Nu*	Empirical (Bowden)
ω=0 *rad/s* ΔT=4*K*	10.21	10.92 ±0.54
ω=0 *rad/s* ΔT=10*K*	14.18	13.74 ±0.68

Table 5: Comparison of empirical with computed Nu for $\omega = 0$.

Conclusions

The numerical model presented here is able to reveal the fundamental aspects of the flow in a wall heated, cylindrical annulus, although some discrepancies with experimental data exist in the velocity field. First, the magnitude of the velocity field is over predicted, and second, the sense of rotation of the lower azimuthal cell is reversed. However, the model behaves logically: there is a symmetrical temperature field and no azimuthal flow for $\omega = 0$; there is no velocity at all for ΔT=0. Also, heat transfer predictions are comparable with experimental results. A weak azimuthal pressure gradient and a larger radial pressure gradient are predicted, as hypothesized by Bowden and Eden[9]. Radial and azimuthal

geostrophic flow take place within the annulus, while the vertical motion is dominated by buoyancy forces.

Guidelines for further work include solving implicitly the conservation equations which would allow larger time steps and reduce computational time. Previous calculations with finer grids[16] showed that the predicted velocity and temperature fields were independent of the grid size. However, no investigations have been carried out to analyze the influence of mesh size in the prediction of transition to the eddy regime.

The numerical scheme is formally first order accurate. A second order accurate scheme could be implemented, although this would imply large changes to the computer code. Implementing the complete conservation of mass equation in place of $\nabla \cdot \mathbf{V} \approx 0$ could improve results. Furthermore, using a control volume approach to discretize the energy equation would ensure global conservation of energy. It was concluded that for high rotation rates the complete energy equation should be used, since the pressure term and the centrifugal term will increase in magnitude, perhaps to the point where they may no longer be neglected.

Reference

[1] Rayer, Q. G., "An Experimental Investigation of Heat Transfer by Large Scale Motions in Rotating Fluids", Dr of Phil. Thesis, St. Hugh's College, Oxford, UK, Mar. 12, 1992.

[2] Mukira, D. T., Precilla, G. and Glakpe, E. K. , "Finite Difference Analysis of Three Dimensional Natural Convection in Non-Orthogonal Coordinates", AIAA Paper 94-1972, June 1994, page 1.

[3] Read, P. L., "The dynamics of rotating fluids: the 'philosophy' of laboratory experiments and studies of the atmospheric general circulation", Meteorological Magazine, Vol. 117 No.1387, Feb. 1988, pp. 35-36.

[4] Fowlis, W. W. and Hide, R., "Thermal Convection in a Rotating Annulus of Liquid: Effect of Viscosity on the Transition Between Axisymmetric and Non-Axisymmetric Flow Regimes", Journal of the Atmospheric Sciences, Vol. 22, Sept. 1965, pp. 541-553.

[5] Williams, G. P., "Thermal Convection in a Rotating Fluid Annulus: Part 1. The Basic Axisymmetric Flow", Journal of the Atmospheric Sciences, Vol. 24, Mar. 1967, pp. 144-160.

[6] Busse, F. H., "Thermal Instabilities in Rapidly Rotating Systems", Journal of Fluid Mechanics, Vol. 44, part 3, 1970, pp. 441-460.

[7] Robinson, A. R. "The Symmetric State of a Rotating Fluid Differentially Heated in the Horizontal", Journal of Fluid Mechanics, Vol. 6, 1959, pp. 599-620.

[8] Bowden, M. and Eden, H. F., "Thermal Convection in a Rotating Fluid Annulus: Temperature, Heat Flow, and Flow Field Observations in the Upper Symmetric Regime", Journal of the Atmospheric Sciences, Vol. 22, 1965, pp. 185-195.

[9] Bowden, M. and Eden, H. F., "Effect of a Radial Barrier on the Convective Flow in a Rotating Fluid Annulus", Journal of Geophysical Research, Vol. 73, Nov. 15, 1968, pp. 6887-6895.

[10] Fultz, D et al "Studies of Thermal Convection in a Rotating Cylinder with some Implications for Large-Scale Atmospheric Motions" Meteorological Monographs, Vol. 4 No. 21. Published by the American Meteorological Society, Dec. 1959, pp. 101.

[11] White, F. M., "Viscous Fluid Flow, 2nd ed." McGraw-Hill, NY, 1991, pp. 59-75 and 574-577.

[12] Reference [11], page 73.

[13] Reference [10], page 17.

[14] Robinson, A. R., "The Symmetric State of a Rotating Fluid Differentially Heated in the Horizontal", Journal of Fluid Mechanics, Vol. 6, 1959, pp. 599-620.

[15] Randriamampianina, A., Bontoux, P. and Roux, B., "Ecoulements Induits par la Force Gravifique Dans Une Cavité Cylindrique en Rotation". International Journal of Heat and Mass Transfer, Vol. 30, No. 7, 1987, pp. 1275-1292.

[16] Ahmed, S., Sherlock, B. G. and Rayer, Q. G., "Numerical Prediction of Three-Dimensional Thermally Driven Flows in a Rotating Frame", Notes on Numerical Fluid Mech., Vol. 53, 1996, pp. 1-7.

[17] Anderson, D. L., Tannehill, J. C. and Pletcher, R. H. Computational Fluid Mechanics and Heat Transfer, pp. 515-517. 249. Hemisphere Publishing Corp., New York 1984.

Appendix:

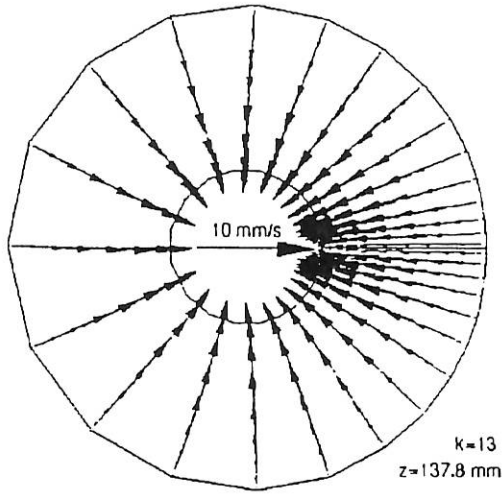

Figure A.1: Velocity vector plot on (r, θ) plane for ω = 0 and ΔT = 10.

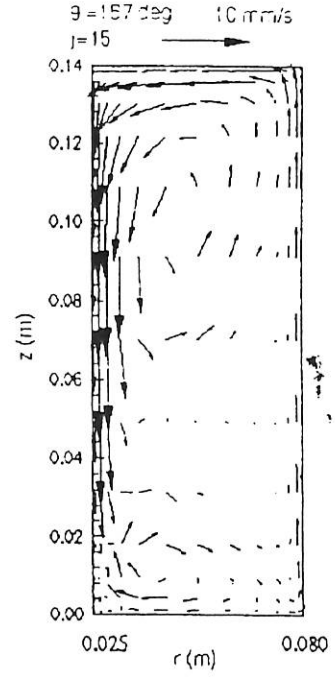

Figure A.2: Velocity vector plot on (r, z) plane for ω = 0 and ΔT = 10.

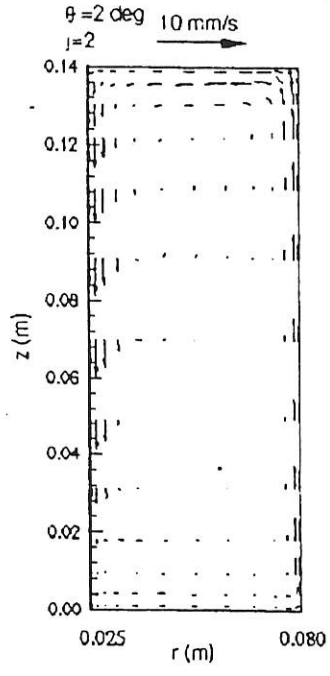

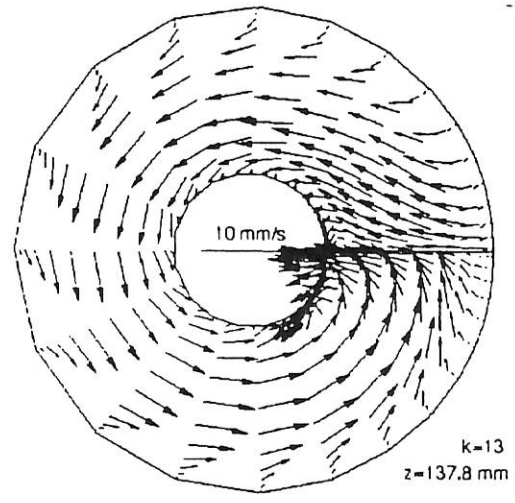

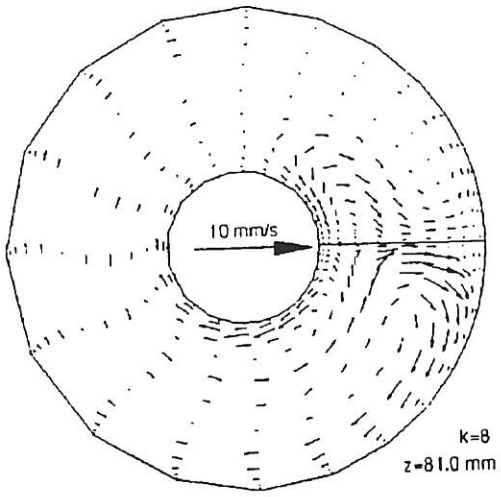

Figure A.3: Velocity vector plot on (r, θ) plane for ω = 0.4 and ΔT = 10.

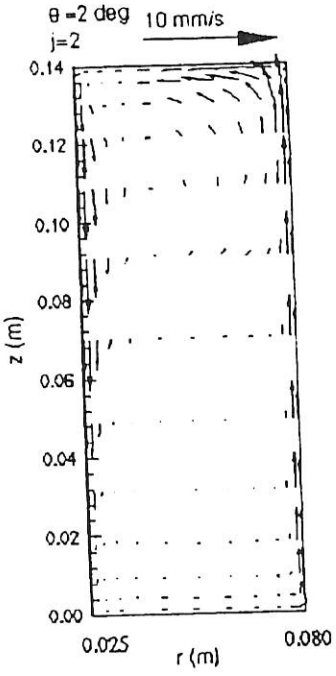

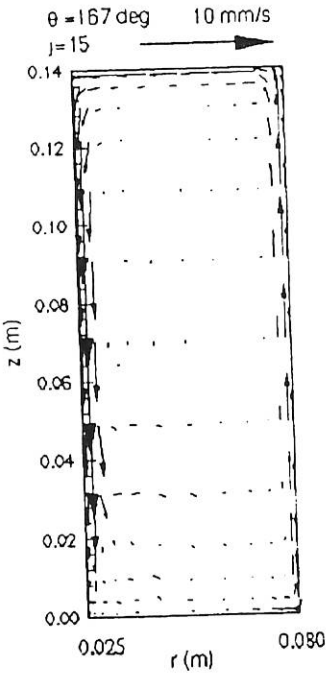

Figure A.4: Velocity vector plot on (r, z) plane for ω = 0.4 and ΔT = 10.

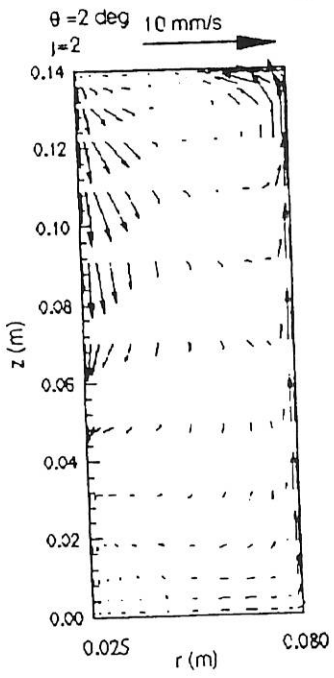

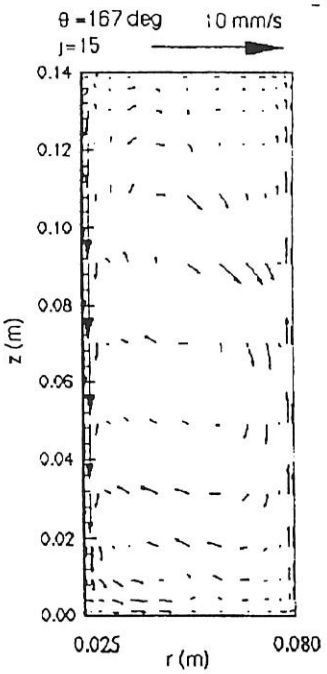

Figure A.5: Velocity vector plot on (r, z) plane for ω = 4 *rad/s* and ΔT = 10 K.

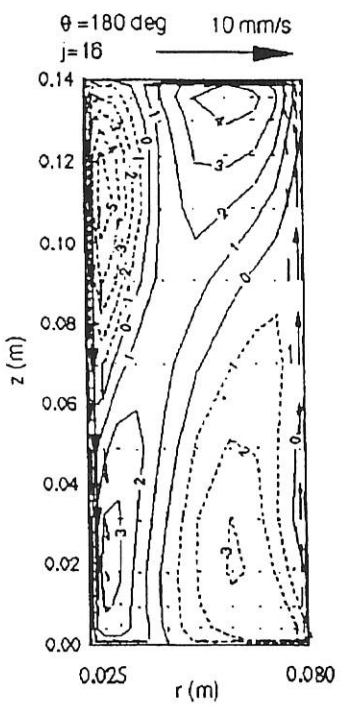

Figure A.6: Azimuthal velocity contours (in *mm/s*) for θ =180° (opposite the radial barrier) overlayed on velocity vector plots. Dashed contour lined indicate negative values. (ω =1.2 *rad/s* ΔT = 10 K)

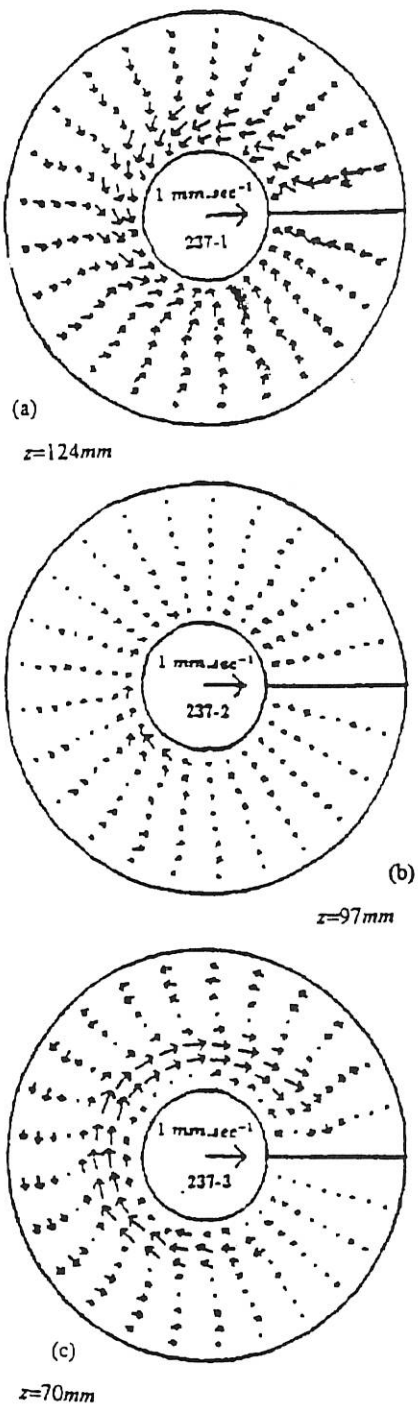

Figure A.7: Experimental Velocity measurements on the (r,z) plane at various values of z for $\omega \approx 0.4$ rad/s and $\Delta T \approx 10$ K, from Rayer [1]. Arrow in center of annulus indicate a velocity of 1 mm/s. Experimental errors in the horizontal velocities is ±0.09 mm/s.

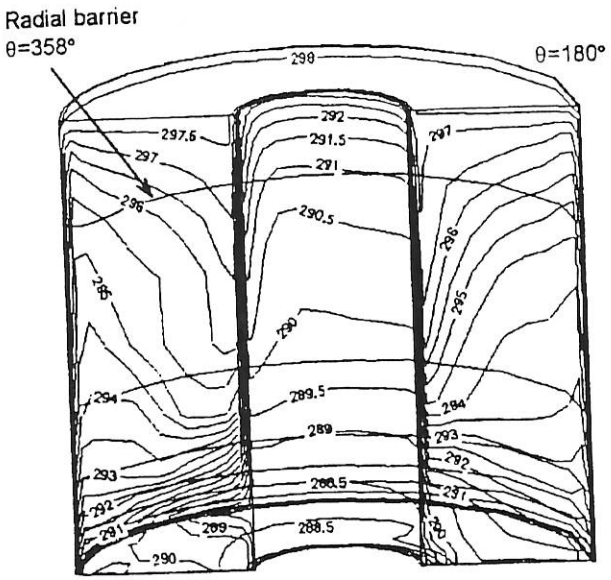

Fig. A.8: ω=0.4 *rad/s* and ΔT = 10 *K*.

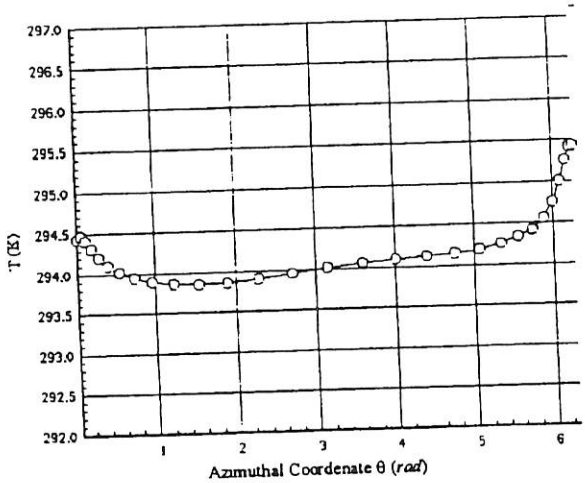

Figure A.9: Temperature at mid-heigth and mid-radius for ω = 0.4, ΔT = 10 *K*.

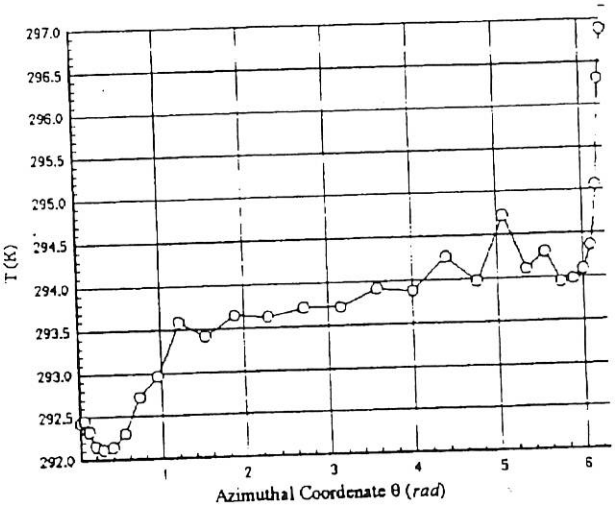

Figure A.10: Temperature at mid-heigth and mid-radius for ω = 4, ΔT = 10 *K*.

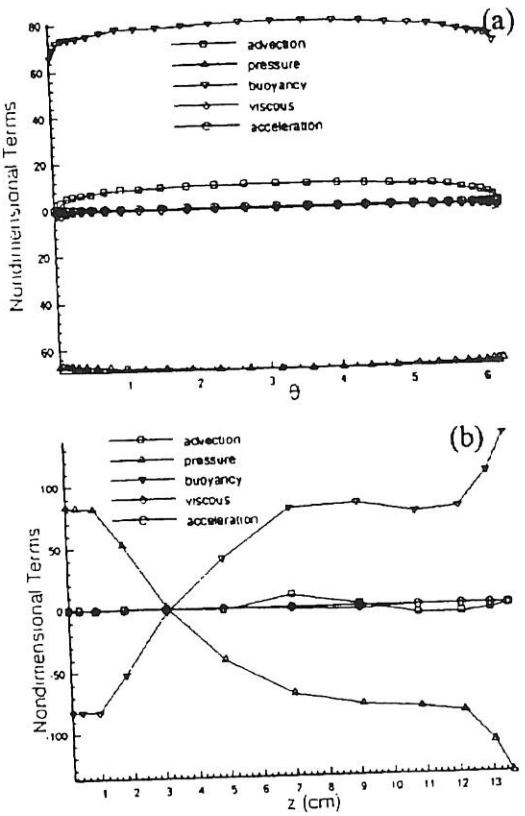

Figure A.11:Vertical components of momentum equation at z=L/2 and θ = 180° as a function of: (a) θ (b) z. (ω = 0 *rad/s*, ΔT=10 K)

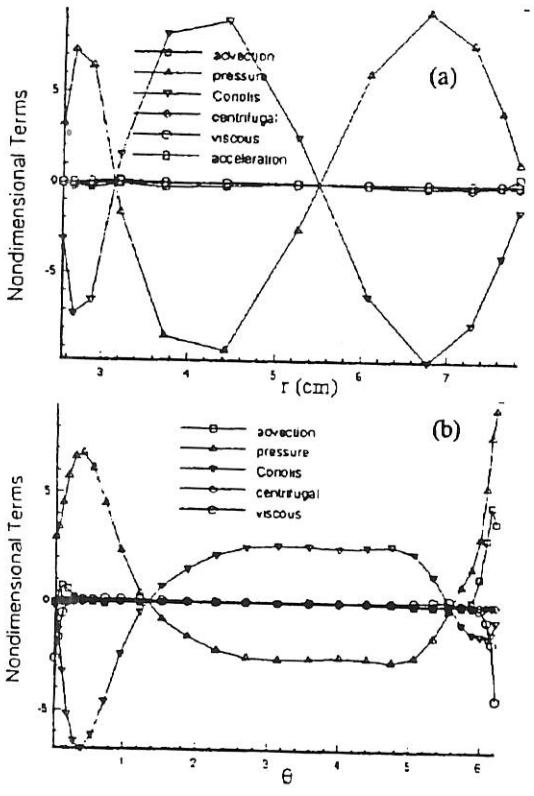

Figure A.12: Radial components of momentum equation at $z = L/2$ and $\theta = 180°$ as a function of: (a) r (b) θ. Geostrophic balance predominates in the body of the fluid, away from boundaries.
$\omega = 0.4$ *rad/s*, $\Delta T = 10$ *K*

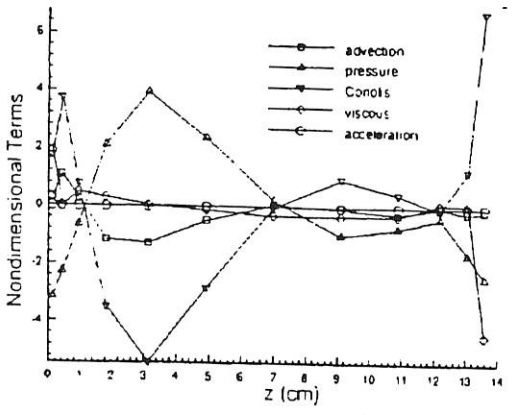

Figure A.13: Azimuthal velocity components at z=L/2 and $\theta = 180°$ as a function of: z.
$\omega = 0.4$ rad/s, $\Delta T = 10$ K

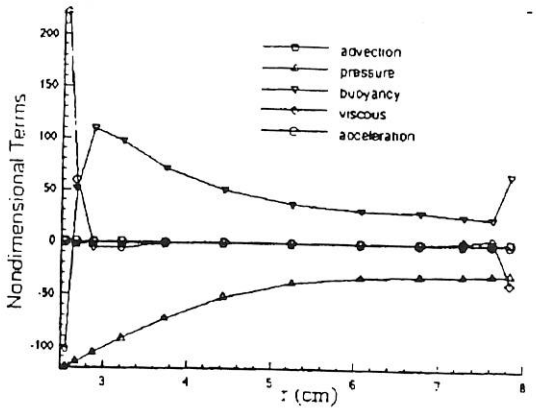

Figure A.14: Vertical velocity components at z=L/2 and $\theta = 180°$ as a function of r.
$\omega = 0.4$ rad/s, $\Delta T = 10$ K

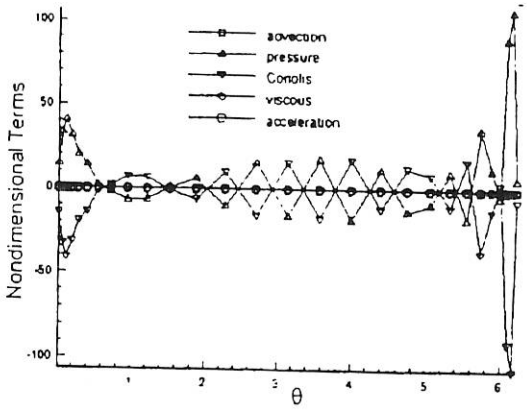

Figure A.15: Azimuthal velocity components at $z=L/2$ and as a function of θ. ($\omega = 4$ *rad/s*, $\Delta T = 10$ *K*)